Chinese Chemical Letters 34 (2023) 107775

Contents lists available at ScienceDirect

Chinese Chemical Letters

journal homepage: www.elsevier.com/locate/cclet

Recent status and future perspectives of $ZnIn_2S_4$ for energy conversion and environmental remediation

Mengzhu Li[a], Longlu Wang[a,*], Xinyu Zhang[c], Weinan Yin[a], Yingbo Zhang[a], Jingwen Li[a], Ziyang Yin[a], Yuntao Cai[a], Shujuan Liu[b], Qiang Zhao[a,b,*]

[a] College of Electronic and Optical Engineering and College of Flexible Electronics (Future Technology), Nanjing University of Posts and Telecommunications (NUPT), Nanjing 210023, China
[b] State Key Laboratory of Organic Electronics and Information Displays and Jiangsu Key Laboratory for Biosensors, Institute of Advanced Materials (IAM), Nanjing University of Posts and Telecommunications, Nanjing 210023, China
[c] School of Geographic and Biologic Information, Nanjing University of Posts and Telecommunications, Nanjing 210023, China

ARTICLE INFO

Article history:
Received 11 July 2022
Revised 30 July 2022
Accepted 22 August 2022
Available online 27 August 2022

Keywords:
$ZnIn_2S_4$
Photocatalysis
Energy conversion
Environmental remediation
Hydrogen evolution

ABSTRACT

Zinc indium sulfide ($ZnIn_2S_4$), a novel photocatalyst, has attracted considerable attention and been extensively studied over the past few years owing to its various advantages such as nontoxicity, structural stability, easy availability, suitable band gap and fascinating photocatalytic activity. This review mainly focuses on the recent state-of-art progress of $ZnIn_2S_4$-based photocatalysts. First, we briefly introduced preparation methods of $ZnIn_2S_4$ with diverse morphological structures. Then, considering the photocatalytic activity of pristine $ZnIn_2S_4$ would be confined by rapid recombination of photo-generated electron-hole pairs and limited light absorption range, different modulation strategies such as layer and size control, doping, vacancy engineering and hetero-nanostructures were expounded in detail. Afterwards, the applications of $ZnIn_2S_4$ in various fields such as H_2 production, CO_2 reduction, value-added products synthesis, pollutant purification and N_2 fixation are clearly summarized. In the end, we sorted out the conclusions and outlook, aiming to provide some new insights for this fascinating material.

1. Introduction

Nowadays, the rapid development of industrialization and worldwide population growth inevitably bring about severe environmental pollution and non-renewable energy shortage. Currently, photocatalytic technology has been generally considered as an effective and sustainable approach to solving these problems [1]. Generally, an ideal photocatalyst needs to have a suitable bandgap, wide light absorption range, high carrier separation efficiency and excellent physiochemical stability. In this aspect, transition metal compounds exhibit great potential in catalysis [2,3]. To date, researchers have developed numerous photocatalysts such as metal oxide (TiO_2 [4,5], WO_3 [6,7]), metal chalcogenides (ZnS [8], CdS [9], MoS_2 [10–12]), metal nitrides [13], and graphitic carbon nitride (g-C_3N_4 [14–16]). However, their photocatalytic performance is usually limited by unsuitable electronic structure and optical properties, which would lead to unwanted recombination of photo-generated electron-hole pairs and limited light harvesting capability. Therefore, researches on semiconductor photocatalysts with more desirable catalytic activity have always been the key to photocatalysis. For example, Zhou *et al.* [17,18] creatively constructed 3D-MoSSe/$NiSe_2$ and $NiSe_2$/Ni foam to produce hydrogen efficiently.

Zinc indium sulfide ($ZnIn_2S_4$), a typical AB_2X_4 family semiconductor, has become a new hotspot in recent years. It has three major crystal structures of hexagonal, cubic and trigonal phase [19], with hexagonal $ZnIn_2S_4$ exhibiting the best photocatalytic behavior [20,21].

Compared with conventional TiO_2 which only absorbs ultraviolet light [22] and has a broad bandgap of approximately 3.05 eV [5], $ZnIn_2S_4$ has superior light harvesting capability in the visible region [23] and a narrower bandgap. Take hexagonal $ZnIn_2S_4$ as an example, its conduction band and valence band position are −0.85 V *vs.* NHE and 1.56 V *vs.* NHE, respectively [24], which is suitable for many redox reactions such as photocatalytic water splitting where the reduction potential of H^+/H_2 is 0 V *vs.* NHE (pH 0) and the oxidation potential of O_2/H_2O is 1.23 V *vs.* NHE (pH 0) [25]. Moreover, $ZnIn_2S_4$ is a bimetallic sulfide mainly

* Corresponding authors at: College of Electronic and Optical Engineering and College of Flexible Electronics (Future Technology), Nanjing University of Posts and Telecommunications (NUPT), Nanjing 210023, China.
E-mail addresses: wanglonglu@njupt.edu.cn (L. Wang), iamqzhao@njupt.edu.cn (Q. Zhao).

https://doi.org/10.1016/j.cclet.2022.107775
1001-8417/

obtained by incorporating zinc into indium sulfide [26] and has no toxicity in comparison with other monometallic sulfide such as CdS [27]. Besides, its stable S-Zn-S-In-S-In-S lamellar structure makes it easier to be modified and construct heterostructures with other materials [28–30], exhibiting great application potential in various fields such as photocatalytic water splitting [31,32], carbon dioxide reduction [26,33], pollutant removal [34,35], nitrogen fixation [36] and sensors [37]. As a result, it is of great significance to summarize the recent advances of $ZnIn_2S_4$-based photocatalysts.

Herein, we first gave the concrete preparation process of $ZnIn_2S_4$ with diverse morphological structures. Then, considering the photocatalytic performance of pristine $ZnIn_2S_4$ is still far from satisfactory and cannot meet the actual demand due to its slow carrier transfer kinetics and adverse electron-hole recombination, various modulation strategies such as layer and size control, doping, vacancy engineering, co-catalyst loading and heteronanostructures were elucidated clearly. Thereafter, several important applications of $ZnIn_2S_4$ were summarized comprehensively. At last, we discussed the conclusion and give our personal outlook. We sincerely hope this review can provide some new ideas for researchers to further promote the development of this fascinating material.

2. Preparation

Till now, the common methods for preparation of $ZnIn_2S_4$ mainly include hydrothermal method [23], solvothermal method [38], spray pyrolysis method [39], chemical vapor deposition method [40], microwave heating method [41], *etc.* Among them, hydrothermal and solvothermal methods have been the most studied owing to their relative mild reactive condition and controllability.

By virtue of regulating temperature, solvent and surfactant, $ZnIn_2S_4$ with diverse morphological structures can be obtained and exhibit excellent photocatalytic performance (Fig. 1). For example, as early as 2006, Gou *et al.* [42] proposed a shape-controlled synthesis of $ZnIn_2S_4$ and successfully synthesized $ZnIn_2S_4$ nanowires, nanotubes, nanoribbons and microspheres *via* a facile solvothermal and hydrothermal route. With zinc sulfate, indium chloride, and thioacetamide (TAA) as precursors and pyridine as the solvent, $ZnIn_2S_4$ nanotubes and nanoribbons were fabricated at temperatures above 180 °C and below 160 °C, respectively. With the same reagent and water replacing pyridine, $ZnIn_2S_4$ solid and hollow microspheres were prepared in the presence of cationic surfactant cetyltrimethylammonium bromide (CTAB) and nonionic surfactant polyethylene glycol (PEG), respectively. Additionally, large quantities of $ZnIn_2S_4$ nanowires could also be transformed from $ZnIn_2S_4$ hollow microspheres samples after an ultrasonic dispersion treatment for over 40 min, when the spheres were almost entirely disintegrated. In 2013, Hu *et al.* [43] creatively developed an ion-induced strategy to prepare $ZnIn_2S_4$ nano-rings. First, $NaInS_2$ was transformed into Cu-doped $NaInS_2$ nanosheets (Cu-$NaInS_2$) and the subsequent Kirkendall effect led to the formation of Cu-$NaInS_2$ nanoring. It was found that the Cu species diffused outward faster than the In^{3+} that diffused inward, which led to the thinning in the center of Cu-$NaInS_2$ nanosheet and the formation of a hollow structure finally. Then the Cu-$ZnIn_2S_4$ was fabricated *via* ion exchange reaction between the Na^+ of the as-prepared Cu-$NaInS_2$ nanoring and Zn^{2+}. Their ingenious method provided a template for the preparation of quaternary alloys. The above-mentioned $ZnIn_2S_4$ with various morphological structures opens the door for preparing composite materials with diverse nanostructures and superior photocatalytic performance through increasing specific surface area and active sites, facilitating light-harvesting capacity, improving charge separation efficiency, *etc.*

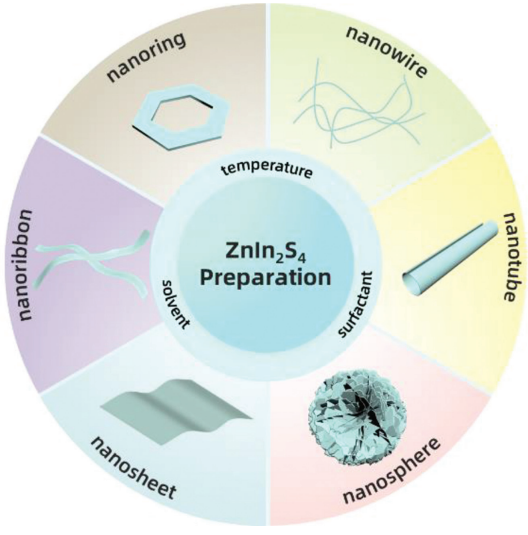

Fig. 1. Schematic diagram of $ZnIn_2S_4$ with different morphologies.

3. Modulation strategies

It is generally known that the photocatalytic activity of pristine $ZnIn_2S_4$ can be limited due to the rapid recombination of electron-hole pairs, sluggish reaction kinetics and poor light absorption capability. Hence, many regulation strategies have been proposed for the sake of achieving superior photocatalytic performance. Herein, we briefly classify these modulation strategies into layer and size control, vacancy engineering, exotic-atom doping, co-catalyst loading and nano-heterostructures (Fig. 2).

3.1. Layer control & size control

Compared with bulk catalyst, ultrathin two-dimensional photocatalysts have many advantages such as stackability, large specific surface area, improved charge migration rate, and high mechanical flexibility [25,44,45]. Therefore, the preparation of ultrathin $ZnIn_2S_4$ nanosheets *via* layer control has been extensively researched. In 2017, Yang *et al.* [46] proposed a self-surface charge exfoliation strategy which briefly involved a facile low-temperature refluxing process and a water-assisted exfoliation treatment by ultrasonication. The as-prepared $ZnIn_2S_4$ nanosheet with a thickness of 2.5 nm proved to be a single-unit-cell atomic layer and is easy to integrate with $MoSe_2$ to form a heterostructure because of elec-

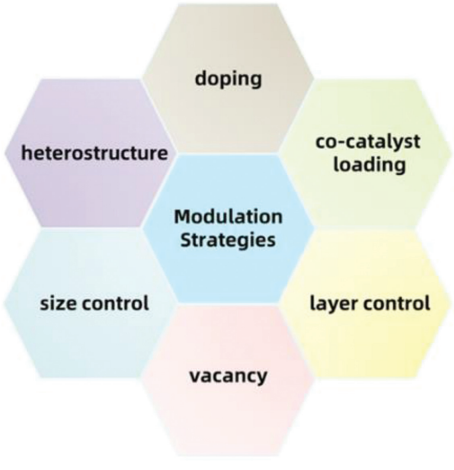

Fig. 2. Schematic illustration of different modulation strategies for $ZnIn_2S_4$.

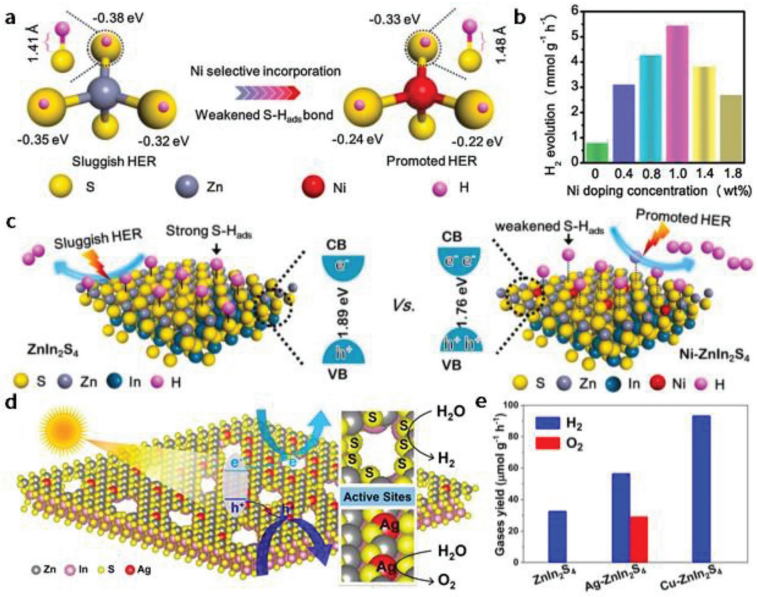

Fig. 3. (a) The adsorption free energy of H of different neighboring S atoms and S-H_{ads} bond length before and after Ni doping. (b) Photocatalytic hydrogen evolution performance of $ZnIn_2S_4$ with different Ni doping quantities. (c) Schematic illustration of photocatalytic hydrogen production process of $ZnIn_2S_4$ and Ni-$ZnIn_2S_4$. Reprinted with permission [52]. Copyright 2021, Elsevier. (d) Schematic depiction of the dual-defect (Ag dopants and nanoholes) formed on $ZnIn_2S_4$ monolayers and the reactive mechanism of the dual-defect structures in photocatalytic overall water splitting. (e) Comparison of the photocatalytic H_2 and O_2 evolution behaviors of $ZnIn_2S_4$, Ag-$ZnIn_2S_4$, and Cu-$ZnIn_2S_4$ under visible light illumination (300 W xenon lamp, $\lambda > 420$ nm). Reprinted with permission [53]. Copyright 2021, American Chemical Society.

trostatic attraction, exhibiting an improved H_2 generation rate of 6454 mmol g^{-1} h^{-1}. This method overcame the drawbacks of lattice mismatching and expensive cost brought by conventional epitaxial growth method and realized independent control of thickness and composition of layer design.

Besides, the size of photocatalysts can determine structural or optical properties and influence photocatalytic process directly. Therefore, researches on preparing $ZnIn_2S_4$ quantum dots with controllable size are of great significance as well. For example, with oleylamine as the ligand and noncoordinating octadecene as the solvent, Peng *et al.* [47] successfully prepared $ZnIn_2S_4$ nanocrystals with tunable size from 2.1 nm to 9.2 nm by temperature control. It was found that the band gap of $ZnIn_2S_4$ increased from 2.35 eV to 3.28 eV with the size decreasing from 9.2 nm to 2.1 nm, which was ascribed to the size-dependent quantum confinement effect. Interestingly, $ZnIn_2S_4$ with a nanoplate structure can also be obtained by replacing the sulfur powder with thiourea as the sulfur source. So far, the accurate control of layer and size of $ZnIn_2S_4$ has not been realized and still needs further study.

3.2. Heteroatom-doping

Doping is an effective strategy to modulate physicochemical properties of $ZnIn_2S_4$ with thickness of atomic level, including extending light absorption range, improving electric conductivity, increasing active sites, adjusting band gap and facilitating the H adsorption and desorption, *etc.* Here we briefly divided the doping strategy into metal doping and nonmetal doping.

3.2.1. Metal doping

Till now, many metal elements such as Cu [48], Mo [49], La [50], Fe [51] have been utilized to modify pristine $ZnIn_2S_4$ to improve its photocatalytic performance. Generally, metal doping can regulate electronic structure, boost carrier separation and extend light absorption spectrum. For example, Qiu *et al.* [52] fabricated Ni-doped $ZnIn_2S_4$ nanosheets with Ni atom substituting Zn atom selectively. In Fig. 3a, the adsorption free energy of H of neighboring S atoms decreased clearly after Ni doping and the S-H_{ad} bonds were longer than before due to Ni incorporation, which facilitated the adsorption and desorption process of H atoms. Besides, the Ni-$ZnIn_2S_4$ exhibited a narrower band gap and an increased density of states (DOS) at valence band maximum (VBM), which contributed to more charge-carriers participating in the photocatalytic reaction (Fig. 3c). Therefore, the hydrogen evolution activity achieved 5.43 mmol g^{-1} h^{-1}, which was almost 7 times as much as that of bare $ZnIn_2S_4$ (Fig. 3b).

Moreover, Pan *et al.* [53] prepared Ag-doped $ZnIn_2S_4$ through a facile aqueous cation exchange reaction between Zn atom of $ZnIn_2S_4$ and Ag^+, which led to the formation of dual defects (Ag dopant and nanoholes). The former boosted photocatalytic oxygen evolution reaction (OER) and the latter facilitated hydrogen evolution reaction in the meantime (Fig. 3d), successfully realizing an all-in-one photocatalytic water splitting (Fig. 3e).

Of note, exotic atoms within photocatalysts can also serve as a recombination center, which is disadvantageous to photocatalytic reactions. For example, Wang *et al.* [54] prepared Cu-doped $ZnIn_2S_4$ with different doping amount to study atomic-level effect of doping on catalytic activity. They found that $ZnIn_2S_4$ with doping quantity of 0.5 wt% exhibited the optimal hydrogen evolution rate of 26.2 mmol h^{-1} g^{-1} while $ZnIn_2S_4$ with doping quantity of 3.6 wt% exhibited a worse photocatalytic performance of 0.9 mmol h^{-1} g^{-1}, compared with pristine $ZnIn_2S_4$ (6.5 mmol h^{-1} g^{-1}). On the one hand, suitable amount of Cu doping can improve light absorption, boost carrier separation and maintain stable coordination structure. On the other hand, excessive Cu doping can lead to the formation of structural distortion and upshift of valence band maximum, which would in turn increase the possibility of electron-hole pairs recombination and worsen photocatalytic behavior.

3.2.2. Nonmetal doping

According to the existing literature, C, O and N elements [55] are three major nonmetal dopants of $ZnIn_2S_4$ nanosheets because they can easily substitute the exposed S atom in the surface of $ZnIn_2S_4$. For example, Xu *et al.* [56] prepared carbon quantum dots doped $ZnIn_2S_4$ nanoflowers with extended light

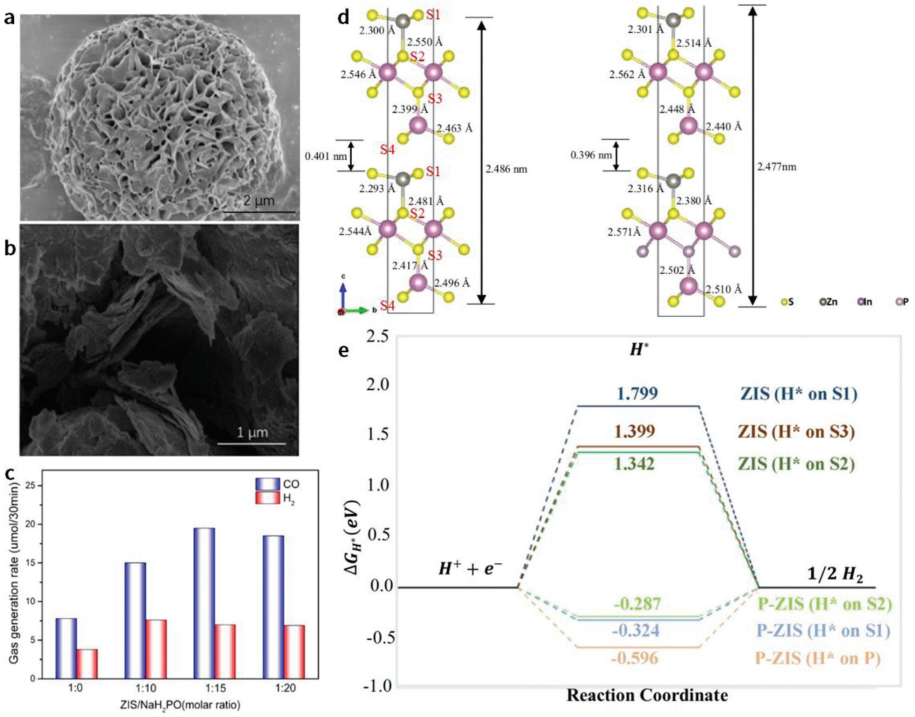

Fig. 4. SEM image of (a) ZIS and (b) P-ZIS. (c) The effect of ZIS/NaH_2PO_4 ratio on the photocatalytic CO_2 reduction. Reprinted with permission [59]. Copyright 2021, American Chemical Society. (d) Simulated crystal structure for pristine ZIS, and P-ZIS (SPD-3). (e) Free energy diagram for hydrogen evolution for each site on ZIS and P-ZIS. Reprinted with permission [60]. Copyright 2022, Springer Nature. To sum up, exotic-atom doping is undoubtedly a pivotal method to enhancing the catalytic activity of $ZnIn_2S_4$ nanosheets: (1) adjust band gap and extend light absorption range; (2) improve electric conductivity; (3) form defects and increase active sites; (4) facilitate reactant adsorption and desorption.

harvesting spectrum, which exhibited improved photocatalytic tetracycline hydrochloride degradation capability. Yang *et al.* [57] fabricated oxygen-doped $ZnIn_2S_4$ where O atoms selectively substituted S atoms in $[ZnS]_4$ tetrahedron and a tremendously boosted hydrogen evolution rate of 2120 μmol h^{-1} g^{-1} was obtained. Du *et al.* [58] synthesized N-doped $ZnIn_2S_4$ and successfully produced hydrogen at 11086 μmol g^{-1} h^{-1}. Recently, it is reported that phosphorus element can serve also as dopant to improve photocatalytic performance of $ZnIn_2S_4$. Qin *et al.* [59] successfully prepared P-doped $ZnIn_2S_4$ *via* a simple hydrothermal method with NaH_2PO_4 as a precursor. Different from pure $ZnIn_2S_4$ microsphere, the as-prepared P-$ZnIn_2S_4$ existed in the form of dispersed ultrathin nanosheets (Figs. 4a and b), which provided enormous exposed specific sites and was beneficial to the CO_2 adsorption process. The optimal P-ZIS with ratio of 1:15 exhibits a CO generation rate of 476 μmol h^{-1} g^{-1}, which was 2.5 times higher than that of pristine $ZnIn_2S_4$ (Fig. 4c). In addition, Chong *et al.* [60] fabricated phosphorus-doped ZIS with P atoms replaced S3 sites exhibiting the best stability (Fig. 4d). They also performed detailed Density Functional Theory (DFT) calculations to unravel the principle of doping effect on photocatalytic water splitting behavior. First, P doping can upshift the valence band maximum and reduce the bandgap of $ZnIn_2S_4$, thus enhancing the light harvesting capability and carrier separation efficiency. Second, owing to the remarkable charge density increase around S2 active sites which are favorable to hydrogen evolution reaction (Fig. 4e), H* adsorption was greatly improved and better hydrogen evolution reaction (HER) performance was achieved.

3.3. Co-catalyst loading

To improve catalytic behavior of pristine $ZnIn_2S_4$, we can also load some co-catalysts on $ZnIn_2S_4$ such as metal atoms, metal sulfides and metal oxides.

Some single atoms with unique electronic structure can greatly regulate absorption intensity and coordination structure of reactants and intermediates, thus promoting catalytic behavior. Metal atoms loaded on $ZnIn_2S_4$ usually possess localized surface plasmon resonance effect and can build Schottky barrier that facilitate light harvesting capability and charge separation, thus endowing $ZnIn_2S_4$ with superior catalytic performance. Pt, Au and Pd are three common metal atoms deposited on $ZnIn_2S_4$. Very recently, Shi *et al.* [61] immobilized Pt atom on hexagonal $ZnIn_2S_4$ nanosheets and successfully produced hydrogen at the rate of 17.5 mmol g^{-1} h^{-1}, with generous H_2 bubbles being observed. That can be ascribed to the synergistic effect of decreased electron-hole recombination and a tip effect induced by Pt single sites. Wang *et al.* [62] rationally loaded Pd atoms on $ZnIn_2S_4$ *via in situ* icing-assisted photo-reduction method. In this case, the Pd atom was coordinated with three sulfur atoms. The introduction of Pd atoms induced charge polarization and provided more active sites. With electrons aggregating around Pd single atoms-ZnS layer and holes distributed to InS_2 layer, the as-prepared Pd-$ZnIn_2S_4$ can effectively realize dual-function of photocatalytic hydrogen evolution (11.1 mmol g^{-1} h^{-1}) and oxidation of benzylamine to *N*-benzylidene benzylamine (10.2 mmol g^{-1} h^{-1}). Feng *et al.* [63] constructed double-metal loaded Au-Pd/$ZnIn_2S_4$, which outperformed Pd/$ZnIn_2S_4$ and Au/$ZnIn_2S_4$ in the oxidation of aromatic alcohol. Moreover, Pan *et al.* [64] successfully anchored Ni atoms in $ZnIn_2S_4$ nanosheets with rich S vacancies. It was found that the incorporation of Ni atoms induced the formation of Ni-O-M (Zn/In) atomic interface, which is favorable for the charge transfer and carrier separation.

Metal sulfides and metal oxides can also be loaded on $ZnIn_2S_4$, which actually forms an 0D-2D heterostructure. For example, Zhang *et al.* [65] ingeniously grew MoS_2 quantum dots at S vacancies on a Zn facet of monolayer $ZnIn_2S_4$ nanosheet, which is obtained *via* a facile bulk $ZnIn_2S_4$ exfoliation and lithium interca-

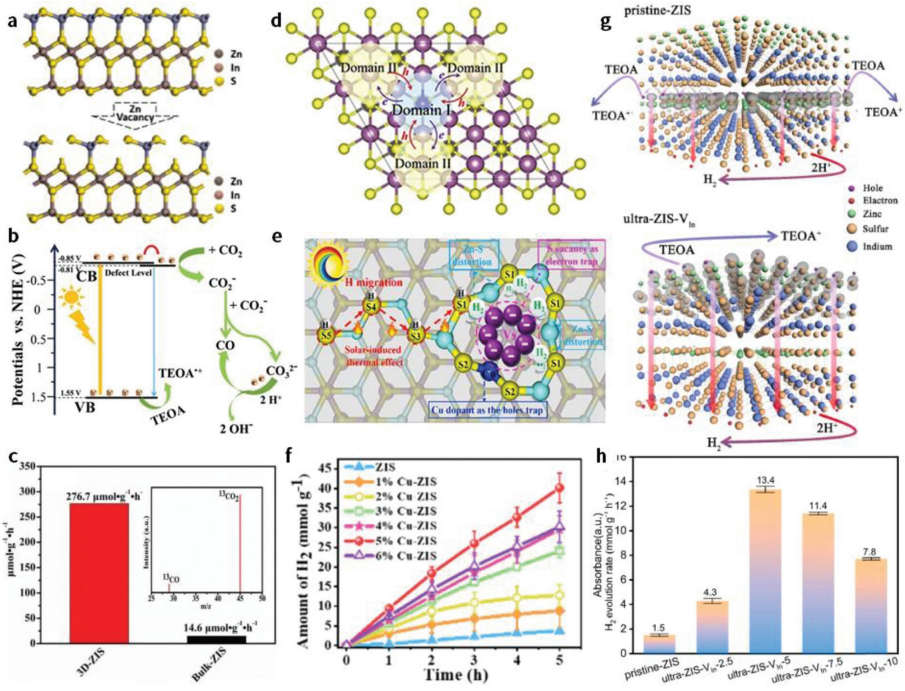

Fig. 5. (a) The schematic illustration of Zn vacancy formation. Reprinted with permission [72]. Copyright 2021, Elsevier. (b) The reactive mechanism of CO_2 reduction for the $ZnIn_2S_4$ with Zn vacancies. (c) The photocatalytic performance of 3D-ZIS with Zn vacancies and bulk-ZIS, respectively. Reprinted with permission [73]. Copyright 2019, Wiley VCH. (d) Schematic diagram of the surface domain potential difference between adjacent microdomains induced by the surface S vacancy defects. Reprinted with permission [74]. Copyright 2022, Elsevier. (e) Schematic depiction of gradient H migration for H_2 evolution of Cu doped ZIS. (f) H_2 evolution activities of ZIS and *x*Cu-ZIS ($x = 1\%$-6%). Reprinted with permission [75]. Copyright 2021, American Chemical Society. (g) Schematic diagram for the photocatalytic hydrogen evolution of pristine-ZIS and ultrathin ZIS-V_{In}. (h) Photocatalytic hydrogen evolution activities of pristine-ZIS and ZIS-V_{In}. Reprinted with permission [76]. Copyright 2022, Elsevier.

lation process. With S vacancies as the electron trap, photogenerated electrons were greatly prevented from transmitting from the Zn facet to In facet and recombing with the holes. And the ultrathin 2D structure also reduced the interlayer resistance and facilitated the charge transfer. Therefore, the photoexcited electrons of V_s-M-$ZnIn_2S_4$ were easy to transfer to MoS_2QDs and participated in hydrogen production. It was found that 2MoS_2QDs@V_s-M-$ZnIn_2S_4$ exhibited the optimal photocatalytic performance (6.884 mmol g^{-1} h^{-1}) and excessive S vacancies can also serve as the recombination center and lower H_2 evolution rate. Notably, there exist some metal sulfides that exhibited the opposite effect. Shen *et al.* [66] and Lim *et al.* [67] found that Ag_2S, SnS, CuS and MoS_2 loading could boost catalytic activity while CoS, NiS or MnS loading hindered the photocatalytic activity of $ZnIn_2S_4$. Zhang *et al.* [28] loaded CeO_2 on $ZnIn_2S_4$ nanosheets through facile solvothermal and room temperature precipitation methods. The highest hydrogen generation rate of the composite reached 847.42 μmol g^{-1} h^{-1}, which is 2.37 times higher than that of bare $ZnIn_2S_4$. Besides, metal oxides like NiO, IrO_2, MoO_2 [68] and ZnO [69] loaded on ZIS have been reported to be favorable to photocatalytic water splitting as well.

Moreover, some other nanoparticles such as $AgIn_5S_8$ [70] and $NiSe_2$ [71] were also well prepared to modify $ZnIn_2S_4$ and boost photocatalysis.

3.4. Vacancy engineering

Atomic vacancy, a typical point defect, forms when some atom breaks away from the bondage of other atoms. Vacancies can improve photocatalytic activity through the following aspects: (1) serve as active site which can trap electrons or holes; (2) extend light absorption range; (3) adjust energy band position and electronic properties; (4) promote adsorption and desorption of intermediate. Zn, S and In are three major vacancies of $ZnIn_2S_4$-based composites.

3.4.1. Zn vacancy

Tai and Zhou [72] introduced Zn vacancies within hierarchical $ZnIn_2S_4$ nanoparticles *via* reactive ion etching technique (Fig. 5a). The as-obtained $ZnIn_2S_4$ had a narrower bandgap and improved cycling stability, thus exhibiting a 2.7-fold enhancement of hydrogen evolution efficiency. He *et al.* [73] also prepared 3D $ZnIn_2S_4$ nanospheres with rich Zn vacancies and conducted carbon dioxide reduction. Zn vacancies introduced a new defect level to capture photogenerated electrons, which facilitated the separation of electron-hole pairs. As shown in Fig. 5b, under light irradiation, electrons and holes are produced in conduction band and valence band, respectively. The photo-excited electrons are further transferred to the defect level instead of recombining with holes and activate CO_2 to generate intermediate CO^{2-} and CO. Eventually, with the synergistic effect of efficient charge separation, increased light response range and more active sites, an enhanced CO_2 reduction rate of 276.7 μmol g^{-1} h^{-1} was achieved (Fig. 5c).

3.4.2. S vacancy

Liu *et al.* [74] prepared defective $ZnIn_2S_4$ microspheres with rich S vacancies *via* a solvothermal method and a low-temperature hydrogenation route. As shown in Fig. 5d, the introduction of S vacancies narrowed bandgap and induced surface domain potential difference which improved light harvest capability and promoted electrons to transfer from S vacancies to adjacent favorable domain and facilitated spatial electron-hole separation. Therefore, the defective $ZnIn_2S_4$ microspheres outperformed pristine $ZnIn_2S_4$ without S vacancies. Zhang *et al.* [75] introduced hetero-atom Cu elaborately *via* substituting the Zn atom of ZIS. Due to electron nonequilibrium and lattice mismatch caused by Cu confinement, a self-adapting S vacancy was induced because of Jahn-Teller distortions

(Fig. 5e). Atomic Cu and V_s synergistically modulate charge separation with V_s being an electron trap and Cu acting as a hole trap. Besides, regulated by V_s and driven by photo-thermal effect, an efficient channel of gradient H migration was constructed. The optimum 5%Cu-ZIS nanosheets with S vacancy exhibit remarkable photo-catalytic HER performance compared with pristine $ZnIn_2S_4$ (Fig. 5f). Besides, Wang *et al.* [76] elaborately synthesized a sulfur-deficient $ZnIn_2S_4$/oxygen-deficient WO_3 composite with C-wood as a photothermal substrate. S and O vacancies improved carrier utilization and light absorption behavior, promoting $ZnIn_2S_4$ and WO_3 to produce hydrogen and oxygen, respectively. Moreover, C-wood as an electron bridge also induced photothermal effect which transformed liquid water into water vapor and was more conductive to water splitting. Under these synergistic effects, this photocatalytic system exhibited 169.2 and 82.5 μmol/h for H_2 and O_2 production, respectively.

3.4.3. In vacancy

Very recently, Luan *et al.* [77] innovatively prepared ultrathin $ZnIn_2S_4$ nanosheets with interlayer In vacancies *via* a heating-up hydrothermal process. According to the electron paramagnetic resonance (EPR) spectra, a greater peak intensity that confirms the presence of defects in ultra-ZIS-V_{In} nanosheets can be clearly observed.

In Fig. 5g, for the pristine ZIS, electrons transferred to the surface $[InS]_4$ tetrahedron from interlayer $[ZnS]_4$ tetrahedron under light irradiation, while the holes were still generated in the interlayer $[ZnS]_4$ tetrahedron. In contrast, for the ultra-ZIS-V_{In}, photogenerated electrons were excited to the surface $[InS]_4$ tetrahedron and holes were generated on the surface $[ZnS]_4$ tetrahedron because the introduction of In vacancies led to the S 3p orbitals near the edge of valence band transferring from the interlayer $[ZnS]_4$ tetrahedron to the surface $[ZnS]_4$ tetrahedron. As a result, ZIS with In vacancies exhibited higher carrier separation efficiency and a fantastic HER performance of 13.4 mmol h^{-1} g^{-1}, which is 8.9 folds higher than that of defect-free $ZnIn_2S_4$ (Fig. 5h). Generally, In vacancies are difficult to realize due to the steric hindrance caused by its location in the interlayer of $ZnIn_2S_4$ stacking structure.

3.5. $ZnIn_2S_4$ hetero-nanostructures

By integrating two materials in one, we can obtain many composites with fascinating properties, which are determined by the hetero-junctions formed between interfaces. Generally, hetero-junctions can be divided into type I heterojunction (straddling bandgap), Type II heterostructures, p-n heterojunction, Schottky junction and Z-scheme heterojunction [78]. According to the morphology of different materials, we concisely classified $ZnIn_2S_4$ hetero-nanostructures into 2D-2D, 1D-2D and 3D nanostructures.

3.5.1. 2D-2D stacking materials

Feng *et al.* [79] synthesized 2D-2D $MoSe_2/ZnIn_2S_4$ *via* a facile a secondary hydrothermal route and the as-obtained composite delivered a HER performance of 1226 μmol g^{-1} h^{-1}. Soon afterwards, Wang *et al.* [80] innovatively fabricated a 2D-2D S_v-$ZnIn_2S_4/MoSe_2$ heterostructure by adding monohydrate ($N_2H_4{\cdot}H_2O$) in the process to form S vacancies which facilitated charge separation and could serve as anchoring sited for Mo atoms. Such structure followed a typical Z-scheme mechanism and exhibited an extraordinarily high hydrogen evolution rate of 63.21 mmol g^{-1} h^{-1}. Su *et al.* [30] constructed $Ti_3C_2T_x/ZnIn_2S_4$ heterostructure to enhance hydrogen evolution. With S vacancies as the electron trap and $Ti_3C_2T_x$ as the electron acceptor, the as-prepared material shortened carrier transfer distance and thus made it easier for electrons transferring to $Ti_3C_2T_x$ and participating in HER. Moreover, the Schottky barrier which formed after contact also suppressed the recombination of electron-hole pairs. Finally, a high hydrogen evolution rate of 148.4 μmol/h was obtained. Additionally, Qin *et al.* [81] prepared a $ZnIn_2S_4/g\text{-}C_3N_4$ 2D/2D photocatalysts with abundant S vacancies *via* hydrothermal method with $Zn(CH_3COO)_2{\cdot}2H_2O$, $InCl_3{\cdot}4H_2O$ and TAA dispersed ethanol solution. With the large contact area, ameliorated charge kinetics and S vacancies serving as the electron trap, a hydrogen evolution rate up to 6095.1 μmol g^{-1} h^{-1} was realized.

3.5.2. 1D-2D

Generally, 1D-2D heterostructure refers to the growth of 2D materials on 1D nanostructures. As early as 2013, Xu *et al.* [29] fabricated $CdS/ZnIn_2S_4$ nano-heterostructure. The lattice mismatch and bond mismatch made $ZnIn_2S_4$ grow helically on the CdS nanowires, thus widening the surface area. In 2014, Liu *et al.* [82] prepared $ZnIn_2S_4$ nanosheets/TiO_2 nanorods heterostructure arrays for water splitting and the as-designed heterostructure improved current density and decreased onset potential. Recently, Li *et al.* [83] also constructed a $ZnIn_2S_4/TiO_2$ heterostructure in which 2D $ZnIn_2S_4$ were grown on TiO_2 nanofibers *via* a hydrothermal route. This composite exhibited optimal hydrogen production rate of 6.03 mmol h^{-1} g^{-1} with TEOA as sacrificial reagent. Under light irradiation, electrons of $ZnIn_2S_4$ bend the conduction band upward and electrons of TiO_2 downward, hence forming an internal electric field. With electrons on TiO_2 conduction band recombing with holes on $ZnIn_2S_4$ valence band, electrons on $ZnIn_2S_4$ conduction band simultaneously participated in HER, which followed a typical S-scheme heterostructure mechanism.

3.5.3. 3D core-shell nanostructure

Generally, core-shell structure is a closed hollow structure mainly consisting of porous material. Such unique structure is favorable for charge transfer, carrier separation and absorption of reactants in shell [84]. For example, Wang *et al.* [85] fabricated $Co_9S_8@ZnIn_2S_4$ heterostructure cage which possessed large specific area and abundant active sites and delivered a hydrogen-production rate of 6250 μmol h^{-1} g^{-1}. His team also successfully prepared Co/N-Doped graphitic carbon nanocages [86] for HER and realized a more efficient H_2 evolution rate of 11270 μmol h^{-1} g^{-1}. Very recently, Fan *et al.* [87] creatively prepared Ce-doped $ZnIn_2S_4$ tetrakaidecahedron hollow nanocages *via* a facile hydrothermal route with Ce-based metal-organic-frameworks. The tetrakaidecahedron hollow structure and Ce dopant synergistically enlarged the surface area, facilitated light harvesting and improved carrier separation efficiency, therefore contributing to an optimal HER activity of 7.46 mmol g^{-1} h^{-1}. Many other core-shell heterostructures have also been extensively prepared such as hollow $Ti_3C_2@ZnIn_2S_4$ [88], $ZnIn_2S_4/Ta_3N_5$ [89] and $TiO_2@ZnIn_2S_4$ hollow nanospheres [90]. However, despite so much merits above, the closed core-shell structure can also inhibit gas reactants diffusion and mass transfer, which goes against its catalytic activity. Therefore, there is still a long way to go for the design of an elaborate porous ultrathin structure.

4. Applications

As a promising photocatalyst with suitable band gap, $ZnIn_2S_4$ has important applications in various fields such as water splitting, value-added products production, pollutant removal, CO_2 reduction, nitrogen fixation. Fundamental principle of $ZnIn_2S_4$ photocatalysis is very simple. Under light irradiation, electrons are excited to the conduction band and holes are generated on the valence band. Then the photo-generated electrons can be transferred to participate in reduction reactions such as H_2 evolution, CO_2 reduction, and nitrogen fixation. Meanwhile, the photo-generated

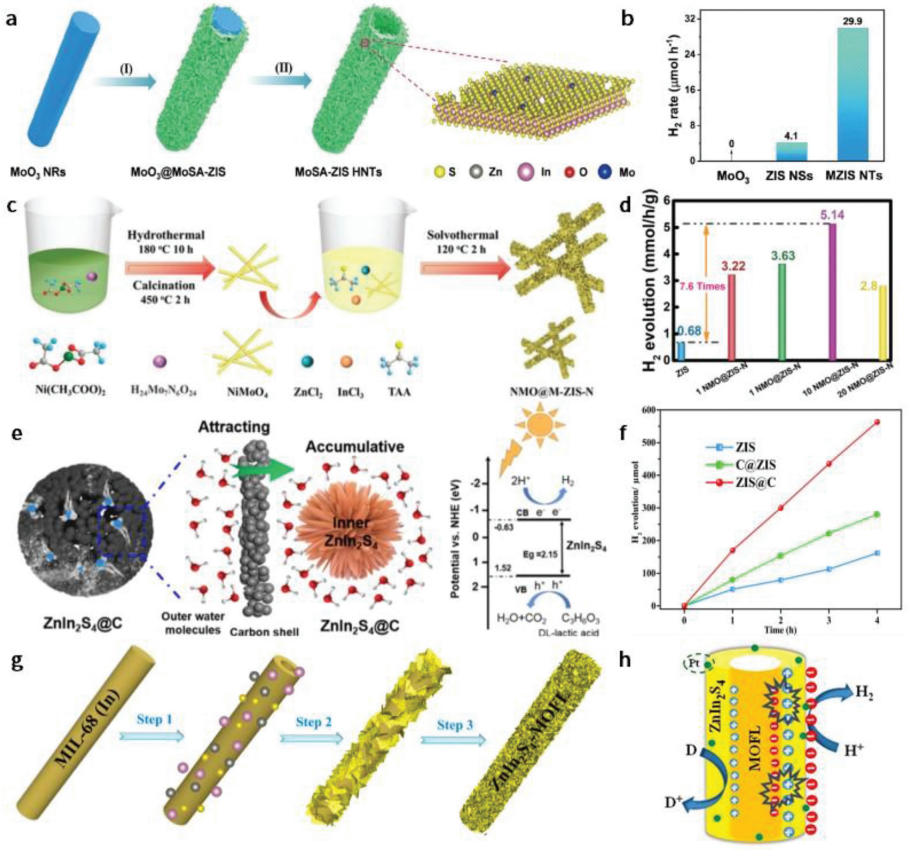

Fig. 6. (a) Schematic diagram of synthetic process for the MoSA-ZIS HNTs photocatalyst. (b) The rates of photocatalytic H_2 evolution over MoO_3 NRs, $ZnIn_2S_4$ NSs and MoSA-ZIS HNTs. Reprinted with permission [91]. Copyright 2021, Springer. (c) Synthetic scheme of NMO@M-ZIS-N. (d) The photocatalytic HER rate of ZIS and NMO@M-ZIS-N with different NMO loading (TEOA as a sacrificial agent). Reprinted with permission [92]. Copyright 2022, The Royal Society of Chemistry. (e) Schematic illustration of the process of capturing the water molecules and a possible photocatalytic mechanism of the HER. (f) Hydrogen evolution activities of ZIS, ZIS@C and C@ZIS ($\lambda \geq 420$ nm). Reprinted with permission [93]. Copyright 2021, American Chemical Society. (g) Schematic illustration for the synthesis of $ZnIn_2S_4$-MOFL. (h) Schematic illustration of photocatalytic mechanism of $ZnIn_2S_4$-MOFL. Reprinted with permission [94]. Copyright 2021, Elsevier.

holes take part in oxidizing reactions such as O_2 production and oxidation of alcohol and benzene.

4.1. H_2 production

Many elaborate designs of $ZnIn_2S_4$-based photocatalysts for HER are constantly emerging these years. Chao and Zhang *et al.* [91] atomically anchored Mo sites on $ZnIn_2S_4$ hierarchical nanotubes (HNTs) through a novel *in-situ* NH_4^+-etched strategy under mild condition (Fig. 6a). Benefited from the mesoporous structure of $ZnIn_2S_4$ HNTs and well-defined Mo-S_2O_1 sites with distinctive coordination configuration, the hollow Mo single-atoms anchored $ZnIn_2S_4$ (MoSA-ZIS) HNTs presented enhanced HER performance of 29.9 μmol g^{-1} h^{-1} compared with $ZnIn_2S_4$ NSs (5.98 μmol g^{-1} h^{-1}) (Fig. 6b). Very recently, Su *et al.* [92] used $ZnIn_2S_4$ to wrap $NiMoO_4$ nanorods through a hydrothermal and solvothermal process (Fig. 6c). During synthesis process, Mo^{5+} was more suitable for doping due to its similar ionic radius to Zn^{2+} and Ni^{2+} was dissolved on $ZnIn_2S_4$ nanosheets. The as-prepared Mo-doped/Ni-supported $ZnIn_2S_4$ nanosheets can successfully realize an optimal hydrogen evolution rate of 5.14 mmol h^{-1} g^{-1} (Fig. 6d). That could be attributed to the synergistic effect of heterojunctions with Mo doping and metallic Ni supports, which extended the light absorption range, enhanced charge transport kinetic, and maintained strong redox capability.

Li *et al.* [93] synthesized a nano-confined $ZnIn_2S_4$@C photocatalyst where ultrathin $ZnIn_2S_4$ nanosheets were capsulated in microporous carbon nanocage (MCN) *via* impregnation and selective etching method.

As shown in Fig. 6e, the hydroxyl functional groups on the outer carbon cages can facilitate the hydrophilicity of ZIS@C, contributing to the water molecules gathering around the external carbon shell. Then, water molecules could be adsorbed inside the nanocavity due to the nanoconfined effect and participated in hydrogen production reaction. Besides, a core-shell structure C@ZIS photocatalyst where the ZIS was coated on the outside of the carbon shell was also prepared for contrast, but its photocatalytic activity only delivered a moderate improvement (Fig. 6f). Zhang *et al.* [94] made use of metal-organic-framework-layers (MOFL) to modify hollow tubular Mo-S_2O_1 sites (Fig. 6g) and surprisingly high HER activity of 28.2 mmol g^{-1} h^{-1}. In Fig. 6h, the photogenerated electrons of MOFL can easily recombined with holes of $ZnIn_2S_4$, leaving photoexcited electrons of $ZnIn_2S_4$ participating in HER with Pt assistance and the holes of MOFL serving as oxidizing agent, respectively.

Recently, Du *et al.* [95] elaborately combined heterojunction effect, cocatalyst effect and photothermal effect in one and successfully prepared Mo_2C/Mo-S_2O_1 sites composite for efficient hydrogen generation. From Fig. 7a, we can clearly observe that the temperature increases as the reaction proceeds. The photothermal effect is especially important for the enhancement of hydrogen evolution rate (22.11 mmol g^{-1} h^{-1}) among the three factors. As shown in Fig. 7b, it is easy for electrons and holes to migrate to the conduction band and valence band of Mo_2C and participate in redox reactions. In Fig. 7c, H_2 generation of both ZIS and MC-ZIS

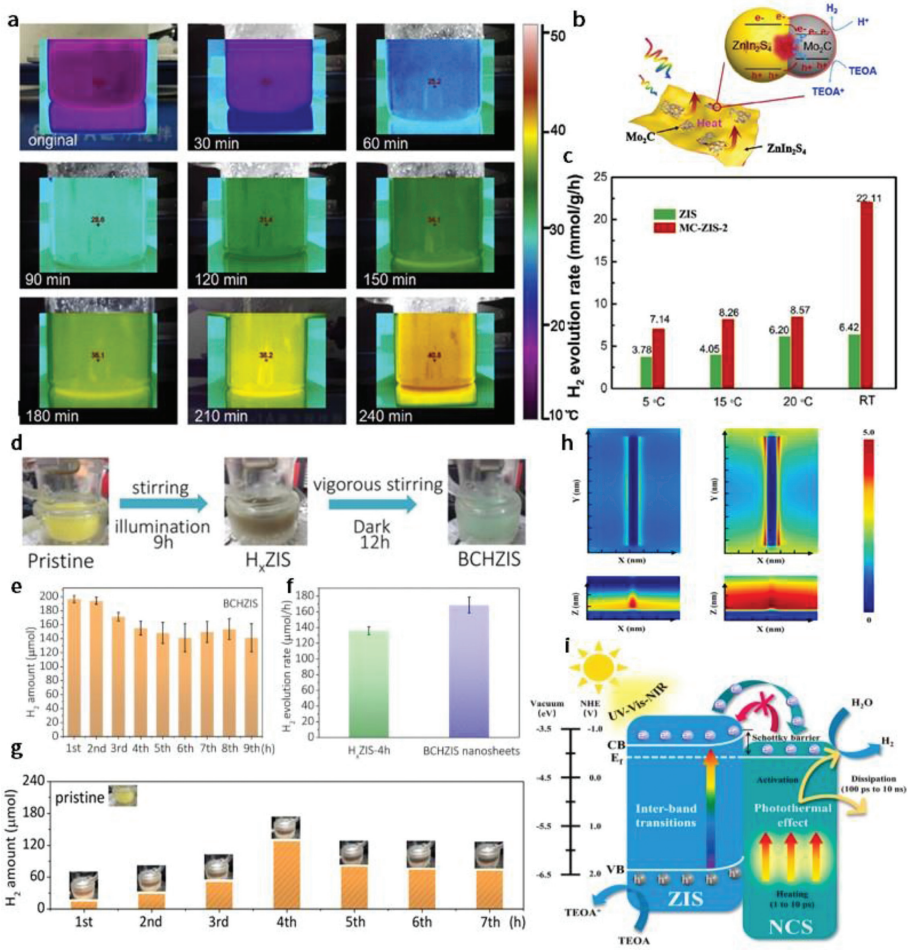

Fig. 7. (a) Photothermal mapping images under visible irradiation in the photocatalytic process. (b) Schematic illustration of the band structure over 2D $ZnIn_2S_4$/amorphous Mo_2C nanoparticles for photocatalytic H_2 generation process. (c) H_2 evolution rates of ZIS and MC-ZIS-2 at different temperature. Reprinted with permission [95]. Copyright 2020, Elsevier. (d) Schematic illustration of hydrogenation process. (e) Photocatalytic H_2 production rate over BCHZIS per hour. (f) Comparison of photocatalytic H_2 production rate between H_xZIS-4h and BCHZIS. (g) Hydrogen evolution amount and the corresponding color change of the ZIS nanosheets. Reprinted with permission [32]. Copyright 2019, Elsevier. (h) FDTD simulation results of NCS/ZIS under wavelengths of 420 nm (left) and 750 nm (right). (i) The possible photocatalytic mechanism of $NiCo_2S_4/ZnIn_2S_4$. Reprinted with permission [96]. Copyright 2022, Elsevier.

increases with the higher temperature and the latter is better than the former overall, which can be ascribed to Mo_2C modification.

Our group [32] creatively proposed a facile hydrogenation method *via* an *in-situ* UV-visible light irradiation for the first time. After 9-h illumination, the H_xZIS was vigorously stirred (1000 r/min, 12 h). The hydrogen evolution amount of bleached ZIS at each hour was illustrated by Fig. 7e. Notably, the color can be bleached within several hours and the bleached $ZnIn_2S_4$ (denoted as BCHZIS) exhibited an efficient and durable photocatalytic hydrogen production rate of 170 μmol/h compared with pristine H_xZIS-4h (about 134 μmol/h) thanks to lower charge-transfer resistance and shorter carrier diffusion pathway induced by H incorporation (Figs. 7d and f). The hydrogen production amount increased in the first 4 h and then decreased and an apparent color change of ZIS from yellow to black was observed (Fig. 7g). The reason for the initial activity decreased after 4 h can be ascribed to the excessive amount of doped H that narrowed the band gap and thus affected reduction ability.

Moreover, Guo *et al.* [96] constructed an intimate contact between noble-metal-free $NiCo_2S_4$ (NCS) and $ZnIn_2S_4$ (ZIS) *via* a two-step solvothermal method and realized 6834.6 μmol g^{-1} h^{-1} compared with pure $ZnIn_2S_4$. The localized surface plasmon resonance (LSPR) effect induced by $NiCo_2S_4$ realized the synergy of near-infrared electric field enhancement and photothermal effect, the former facilitating the rapid transfer of photogenerated electrons and the later boosting the activation of H-OH bond in adsorbed water molecules. According to finite time domain (FDTD) simulated calculation (Fig. 7h), it is easy to observe that the electric field intensity was remarkably strengthened with the increase of incident light wavelength, which is favorable to the charge transfer from ZIS to NCS. A possible mechanism was also proposed in Fig. 7i. Under light irradiation, the photo-excited electrons of ZIS transferred to the conduction band of NCS and produce hydrogen. The Schottky barrier was also formed simultaneously and promote carrier separation.

4.2. CO_2 reduction

Carbon dioxide, a greenhouse gas with massive emission, has caused critical environmental pollution in the past few decades. Efficient reduction of CO_2 to value-added organic matter such as methane and formate is a feasible approach to alleviating this problem.

Recently, Chi *et al.* [26] incorporated zinc in the synthesis of indium sulfide (In_2S_3), successfully obtaining $ZnIn_2S_4$ nanoflowers with hexagonal structure. The as-prepared $ZnIn_2S_4$ catalyst exhibits 99.3% Faradaic efficiency of CO_2 reduction to formate with outstanding stability at 300 mA/cm^2 over 60 h of continuous oper-

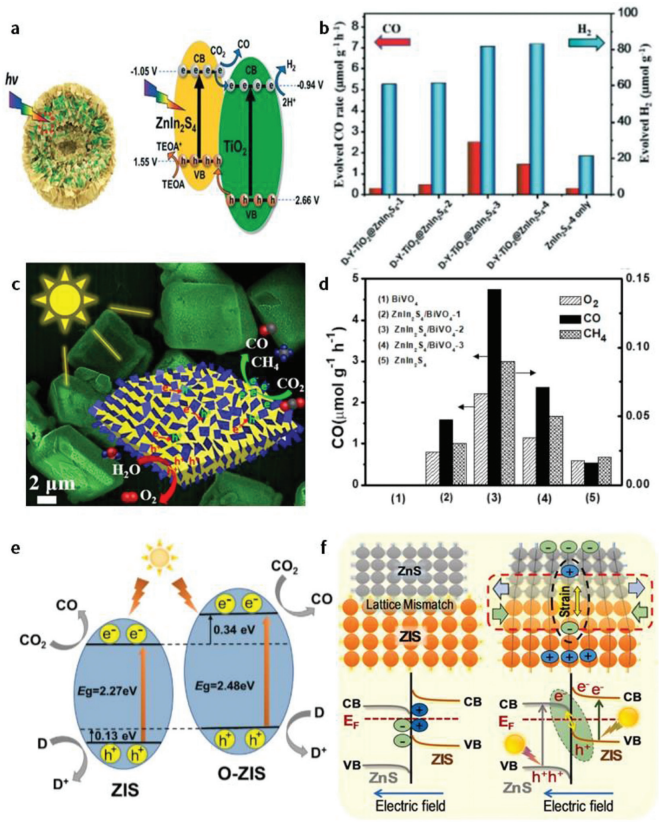

Fig. 8. (a) Possible mechanism of CO_2 reduction with the TiO_2@$ZnIn_2S_4$ photocatalyst. (b) CO/H_2 generation rates of D-Y-TiO_2@$ZnIn_2S_4$ with different loading amounts of $ZnIn_2S_4$. Reprinted with permission [98]. Copyright 2022, The Royal Society of Chemistry. (c) Schematic illustration of the photocatalytic CO_2 reduction for $ZnIn_2S_4$/$BiVO_4$. (d) Comparison of photocatalytic activity over different $ZnIn_2S_4$/$BiVO_4$ samples. Reprinted with permission [99]. Copyright 2021, American Chemical Society. (e) Schematic depiction of mechanism of the pristine ZIS and O-doped ZIS samples. Reprinted with permission [100]. Copyright 2021, Elsevier. (f) Schematic diagram of lattice mismatch and strain effect between cubic ZnS and hexagonal ZIS phases in ZnS/ZIS. Reprinted with permission [101]. Copyright 2022, Elsevier.

ation. In contrast, In_2S_3 without Zn incorporation loses catalytic activity quickly under the same circumstances. Researchers found that Zn introduction improved the covalency of In-S bonds to a large extent, thus locking S catalytic sites which can activate H_2O to react with CO_2 and facilitate he formation of HCOO* intermediates. Besides, Jiao *et al.* [33] prepared one-unit-cell thick $ZnIn_2S_4$ with abundant Zn vacancies to facilitate CO_2 reduction to formate. On the basis of advantages brought by Zn vacancies such as increased charge density and decreased electrochemical impedance, V_{Zn}-$ZnIn_2S_4$ exhibited a CO_2 reduction rate of 33.2 μmol g^{-1} h^{-1} and excellent stability after 24 h. Wang *et al.* [97] constructed a $ZnIn_2S_4$-In_2O_3 hierarchical tubular heterostructure for promoting CO_2 reduction to CO through growing $ZnIn_2S_4$ on the outer and inner surfaces of hexagonal In_2O_3 nanotubes. Such hollow porous tubular heterostructure was conductive to charge transfer and light absorption and realized a CO production rate of 3075 μmol h^{-1} g^{-1}).

She *et al.* [98] prepared spike-like double yolk-shell structure TiO_2@ $ZnIn_2S_4$ for CO_2 reduction to syngas. As shown in Fig. 8a, under light irradiation, the photogenerated electrons of $ZnIn_2S_4$ could be transferred to the conduction band of TiO_2 and participated in the CO_2 reduction and hydrogen evolution reactions. Such an elaborate structure can provide more active sites, improve light absorption and reduce charge transfer path. Additionally, it was also found that the CO_2 reduction activity increased at first and then decreased with $ZnIn_2S_4$ loading amount increasing (Fig. 8b). The optimal reduction performance is 325.29 μmol/g and 227.18 μmol/g for CO and H_2, respectively. Han *et al.* [99] elaborately designed a $ZnIn_2S_4$/$BiVO_4$ hierarchical heterostructure by assembling $ZnIn_2S_4$ nanosheets on $BiVO_4$ decahedron (Fig. 8c) in a hydrothermal and solvothermal route. The as-prepared composite exhibited an enhanced photocatalytic activity for O_2, CO and CH_4 evolution compared with bare $ZnIn_2S_4$ and $BiVO_4$ (Fig. 8d).

Pan *et al.* [100] fabricated O-doped $ZnIn_2S_4$ and achieved a CO evolution rate of 1680 μmol h^{-1} g^{-1} under visible light irradiation, which can be ascribed to the upshift of conduction band (Fig. 8e) and enhanced reduction capability induced by O dopant. Sabbah *et al.* [101] constructed a ZnS/$ZnIn_2S_4$ heterostructure which followed a typical Z-scheme mechanism. As shown in Fig. 8f, the interface lattice mismatch led to a micro-strain, which resulted in electrons in the conduction band of ZnS recombing with holes in the valence band of ZIS. Therefore, the electrons of ZIS and holes of ZnS with better redox capability participated in CO_2 reduction and O_2 production reactions.

4.3. Value-added products synthesis

Oxidation of aromatic alcohols to aromatic aldehydes is a significant organic synthesis process. Heating and suitable catalysts are two prerequisites for reaction to proceed. However, the generation of some unwanted by-products and massive consumption of heating energy are two main problems in practical production. Recently, some $ZnIn_2S_4$-based photocatalysts have been reported to realize highly efficient and selective photocatalytic synthesis of aldehydes.

For example, our group [102] elaborately prepared plasmonic $W_{18}O_{49}$/$ZnIn_2S_4$ photocatalyst to oxidize benzyl alcohol (BA) to benzaldehyde (BAD) selectively. Due to the LSPR effect of $W_{18}O_{49}$, hot electrons are generated and continuously inject into the CB of ZIS, further increasing the electron density and boosting molecule oxygen activation. Besides, photothermal effect brings a quick surface temperature increase (Fig. 9a), synergistically enhancing the reaction rate of BA selective oxidation. Under NIR light irradiation, both $ZnIn_2S_4$ and $W_{18}O_{49}$ can be photoexcited and generate electron-hole pairs. Then the transfer pathway of photoinduced carriers of WOZ heterojunctions follows the Z-scheme mechanism, leaving the highly reductive electrons on the conduction band of ZIS to activate the adsorbed O_2 on photocatalyst surface to produce $^{\cdot}O_2^-$,which participates in the BA selective oxidation (Fig. 9d). The highest conversion efficiency of BA into BAD of WOZ-60 was 3.1 and 18.6 folds of pristine ZIS and $W_{18}O_{49}$, respectively. Similarly, Lu *et al.* [103] combined $ZnIn_2S_4$ nanosheets and hierarchical $W_{18}O_{49}$ micro-flowers, successfully realizing full-spectrum photocatalytic hydrogen evolution. Through density-functional theory calculation, they proposed that the localized electrons around periodic arranged W^{5+}-W^{5+} pairs were the basis reason of LSPR of $W_{18}O_{49}$, which created hot electrons and injected into the conduction band of $ZnIn_2S_4$. Li and Peng *et al.* [104] decorated polypyrrole (PPy) nanotubes with ultrathin $ZnIn_2S_4$ nanosheets *via in-situ* growth method (Fig. 9b). S vacancy With PPy as the electron collector, the as-prepared optimal 10%-PPy@$ZnIn_2S_4$ composite exhibited the best hydrogen evolution rate of 1428 μmol g^{-1} h^{-1} and selective conversion efficiency (98.9%) of 1,4-benzenedimethanol (BDM) to 1,4-phthalaldehyde (PAD) simultaneously (Fig. 9c).

Tan *et al.* [105] prepared $ZnIn_2S_4$ microspheres with MoS_2 as cocatalyst *via* hydrothermal method and photo-deposition method. The HRTEM image (Fig. 9e) clearly confirmed the successful introduction of MoS_2. According to Fig. 9f, ZIS loaded with MoS_2 exhibited superior photocatalytic performance than bare $ZnIn_2S_4$ and the optimal sample is 1%-MoS_2-ZIS (68.8 μmol for H_2 evolution and 70.8 μmol for FAL generation). As shown in Fig. 9g,

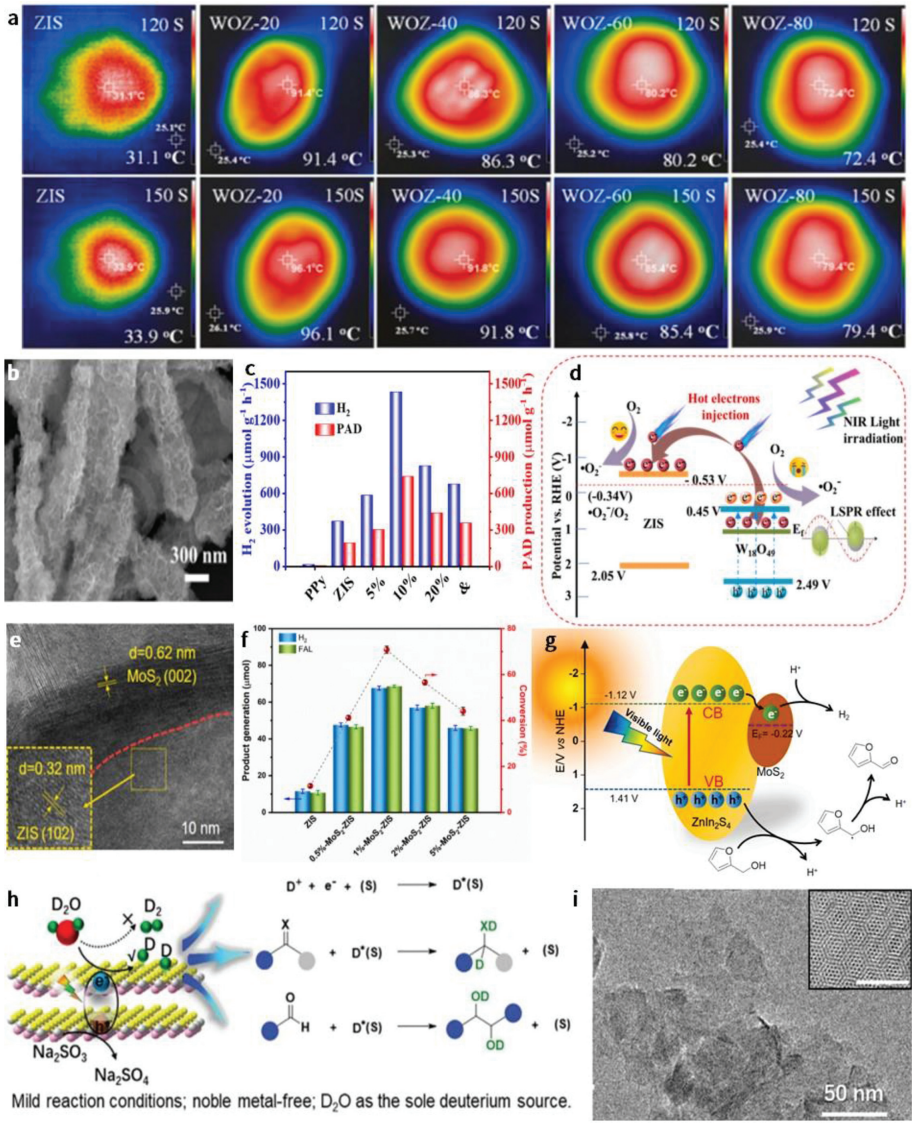

Fig. 9. (a) The infrared photothermal images of different photocatalysts. Measuring conditions: 300 W Xe light (λ>400 nm) with the light intensity of 0.5 W/cm^2. Reprinted with permission [102]. Copyright 2021, Elsevier. (b) FESEM images of 10%-PPy@ZIS. (c) Photocatalytic H_2 evolution and PAD production efficiency of 10%-PPy@ZIS. Reprinted with permission [104]. Copyright 2022, Elsevier. (d) Schematic illustration for the hot electron pathways of the photocatalytic process. Reprinted with permission [102]. Copyright 2021, Elsevier. (e) HRTEM image of MoS_2-ZIS. (f) Photocatalytic performance of prinstine ZIS and MoS_2-ZIS with different amounts of MoS_2. (g) Proposed reaction mechanism for dual reaction for furfuryl alcohol degradation and H_2 evolution over MoS_2-ZIS under visible light irradiation. Reprinted with permission [105]. Copyright 2021, Elsevier. (h) Photocatalytic deuteration of carbonyls to produce alcohols using D_2O as the sole deuterium source. (i) TEM images of D-ZIS. Reprinted with permission [106]. Copyright 2022, John Wiley & Sons, Ltd.

under visible irradiation, the photoexcited electrons on the conduction band of $ZnIn_2S_4$ were transferred to MoS_2 owing to its more positive Fermi level than $ZnIn_2S_4$, therefore facilitating carrier separation. Then, the electrons could easily react with H^+ adsorbed on the MoS_2 surface to produce hydrogen and the holes participated in the oxidation of furfuryl alcohol (FOL) to obtain the value-added product furfural (FAL). Recently, Han *et al.* [106] prepared ultrathin 2D $ZnIn_2S_4$ with plentiful S vacancies assisted with surfactant modification for efficient photocatalytic deuteration of carbonyls to alcohols with D_2O as the deuterium source under mild reaction condition (Fig. 9h). Interestingly, the hexagonal moiré pattern resulting from interference between the crystalline lattices of the stacked nanosheets in D-ZIS could also be observed (Fig. 9i). As we know, a moiré pattern is generally formed when two periodic patterns are overlaid with a relative twist, therefore verifying the formation of ultrathin 2D structure. This research overcame the drawbacks of previous deuteration such as harsh reaction conditions, noble-metal catalysts, and costly deuterium sources.

4.4. Pollutants degradation

Nowadays, with the development of industrialization, the consequent contaminants have become an increasingly serious problem that troubles many countries all around the world. In recent years, the $ZnIn_2S_4$-based photocatalysts have been widely researched by scientific researchers, expected to mitigate the pollution issues.

In 2021, Zhang *et al.* [107] elaborately designed hierarchical Z-scheme Ag_3PO_4@$ZnIn_2S_4$ nanoscoparium through decorating Ag_3PO_4 nanoparticles on the $ZnIn_2S_4$ nanoscopariums (Figs. 10a and b), greatly contributing to tetracycline degradation. The highest tetracycline removal efficiency can reach 92.3% under the optimal component conditions (Ag_3PO_4@$ZnIn_2S_4$-30%) and the system exhibits excellent durability after five successive runs. Additionally, they also detected the reactive oxygen species during the photocatalytic reaction, and found that both superoxide radical ($\cdot O_2^-$) and hydroxyl radical ($\cdot OH$) were involved in the

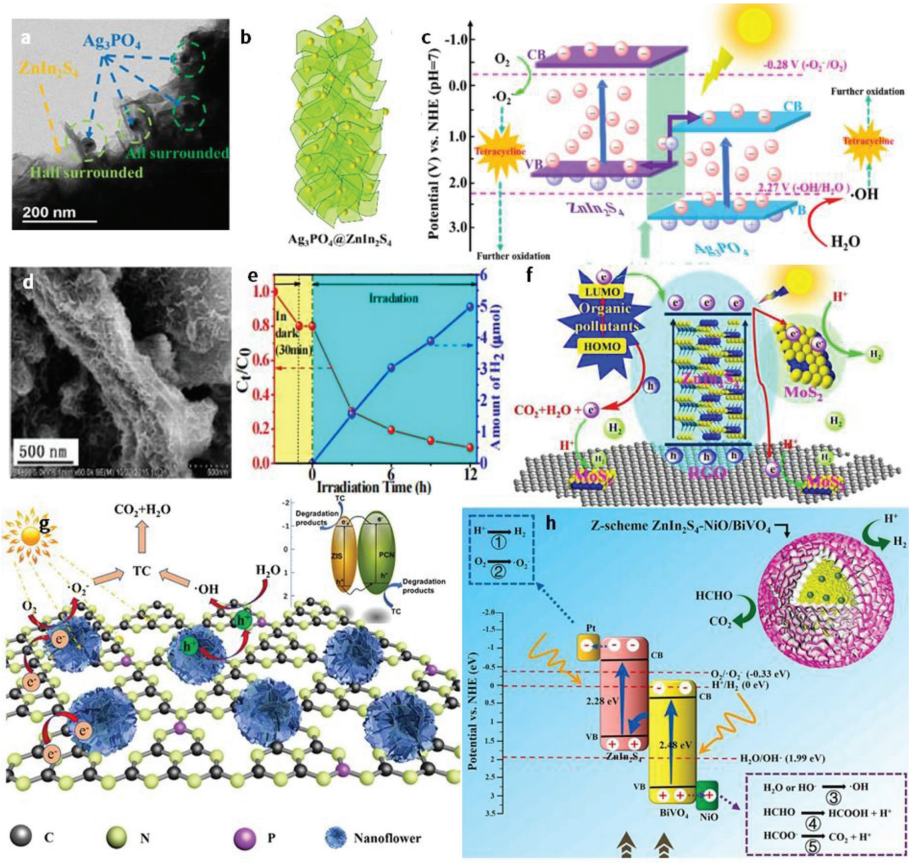

Fig. 10. (a) HRTEM image of Ag_3PO_4@$ZnIn_2S_4$. (b) Structural diagram of Ag_3PO_4@$ZnIn_2S_4$. (c) Photocatalytic mechanism for the degradation of tetracycline on Z-Scheme Ag_3PO_4@$ZnIn_2S_4$ photocatalyst. Reprinted with permission [107]. Copyright 2021, Elsevier. (d) SEM images of 5MoS_2QDs@$ZnIn_2S_4$@RGO1. (e) Simultaneous hydrogen production with PNP degradation. C_t and C_0 are the residue concentration and initial concentration (20 mg/L) in water, respectively. (f) Illustration of electron flow and energy conversion during organic pollutant degradation. Reprinted with permission [35]. Copyright 2017, Elsevier. (g) Schematic depiction of PCN/ZIS photocatalyst. Reprinted with permission [34]. Copyright 2021, Elsevier. (h) Reactive mechanism of photocatalytic H_2 production and simultaneous HCHO degradation of $ZnIn_2S_4$-NiO/$BiVO_4$. Reprinted with permission [108]. Copyright 2021, Elsevier.

photocatalytic reaction, with ·OH playing the leading role. As shown in Fig. 10c, electrons on the conduction band of Ag_3PO_4 recombined with holes on the valence band of $ZnIn_2S_4$, leaving electrons on the conduction band of $ZnIn_2S_4$ and holes on the valence band of Ag_3PO_4 participating in redox reaction more advantageously. Clearly, it followed a typical Z-scheme mechanism. Besides, Zhang *et al.* [35] successfully constructed a MoS_2QDs@$ZnIn_2S_4$@RGO photocatalyst (Fig. 10d), which can not only purify pollutants such as rhodamine B (RhB), eosin Y (EY), fulvic acid (FA), methylene blue (MB) and *p*-nitrophenol (PNP), but also produce hydrogen simultaneously without noble metals as co-catalysts. It is worth noting that these dye molecules can also be photoexcited and provide electrons which were further transmitted to the conduction band of ZIS or RGO. That's why the concentration of organics decreased with prolonged irradiation time, whereas the hydrogen evolution still increased obviously (Fig. 10e). The mechanism is clearly depicted in Fig. 10f. With light irradiation, the photogenerated electrons of $ZnIn_2S_4$ were transferred to RGO (reduced grapheme oxide) and MoS_2QDs to promote hydrogen evolution reaction, while the photogenerated holes were used to oxidize and degrade dye molecules that were adsorbed to catalysts. Zhou *et al.* [34] synthesized Phosphorus-doped g-C_3N_4/$ZnIn_2S_4$ (PCN/ZIS) heterojunction photocatalyst *via* a solvothermal method. Improved by the synergistic effect of heterostructure and P doping (Fig. 10g), an enhanced tetracycline degradation activity of 0.0874/min was realized.

Yang *et al.* [108] successfully constructed a Z-scheme $ZnIn_2S_4$-NiO/$BiVO_4$ hierarchical hetero-junction *via* assembling NiO_2 particles and $ZnIn_2S_4$ nanosheets on the surface successively, thereby achieving highly efficient photo-catalytic hydrogen production and formaldehyde degradation simultaneously. As shown in Fig. 10h, e^- on the CB of $BiVO_4$ are combined with the h^+ on the VB of $ZnIn_2S_4$, which improves redox ability of the photo-catalytic system and promotes separation of photo-generated electron-hole pairs. O_2 concentration, pH and HCHO initial concentration are three main factors that affect catalytic performance. Under the optimal circumstance (80% of O_2, 13 of pH and 1.5 mol/L of HCHO initial concentration), the outstanding H_2 evolution activity and HCHO degradation activity are 2724.89 μmol/h and 17.00 mmol/h, respectively.

4.5. N_2 fixation

Although the nitrogen content in the atmosphere reaches 70%, the nitrogen molecule is very stable, and most organisms cannot directly use it. Therefore, it is of great significance to convert nitrogen in the atmosphere into nitrogen-containing compounds and obtain the nitrogen needed by organisms. $ZnIn_2S_4$ as an efficient photocatalyst has also shown promising behavior in nitrogen fixation. For example, Zang *et al.* [36] constructed 2D/2D $ZnIn_2S_4$/BiOCl heterostructure *via in-situ* solvothermal techniques to optimize N_2 fixation and phenol degradation. In detail, photoexcited electrons of $ZnIn_2S_4$ can activate N≡N bond and generate intermediates such as N_2H^* and species. Finally, $NH_3{}^*$ was combined with H_2O molecules to form $NH_4{}^+$. Besides, Chen *et al.* [109] fabricated a novel core-shell polyaniline@$ZnIn_2S_4$ heterostructure

photocatalysts, with $ZnIn_2S_4$ nanoparticles growing directly on the surface of polyaniline (PANI) nanorods. Benefiting from the strong interfacial interactions, the samples exhibited an increased N_2 photo-fixation performance which is 10 times higher than that of pure $ZnIn_2S_4$.

5. Conclusions and outlook

$ZnIn_2S_4$ is an emerging material with great prospect in the field of photocatalysis and is expected to effectively improve environmental pollution and energy shortage problem. As a ternary chalcogenide semiconductor with a unique lamellar structure, $ZnIn_2S_4$ has various excellent characteristics such as nontoxicity, low cost, suitable energy band structure, desirable photocatalytic performance and good durability. However, photocatalytic performance of bare $ZnIn_2S_4$ is severely confined due to the rapid recombination of electron-hole pairs, sluggish carrier transfer kinetics and limited light absorption range. As a result, many scientific researches have been carried out to enhance photocatalytic performance of pristine $ZnIn_2S_4$. Firstly, element doping, which substitutes exotic atoms for some atoms in $ZnIn_2S_4$ or injects exotic atoms into crystal lattice of $ZnIn_2S_4$, can realize some favorable effects such as increased active sites, narrower band gap, improved electric conductivity and extended light harvest range. Second, vacancy engineering which mainly involves S, Zn and In vacancies and distortions is conductive to increasing charge density, prohibiting electron-hole recombination as well. Additionally, construction of heterostructure like 1D-2D, 2D-2D, and 3D can enlarge specific surface area and shorten charge diffusion path, thus improving charge utilization and photocatalytic performance. To date, by means of those modulation strategies to promote catalytic performance, researchers have realized various kinds of applications in different fields such as hydrogen evolution, CO_2 reduction, nitrogen fixation, value-added products and pollutant removal. Nevertheless, there are still some challenges and drawbacks in the research process. Herein, we sorted out our outlook as follows.

(1) Currently, the most common method to preparing $ZnIn_2S_4$ is limited to hydrothermal or solvothermal approach. Although we can synthesize $ZnIn_2S_4$ with different morphology by changing reaction conditions, the precise control of shape and thickness of $ZnIn_2S_4$ is still not achieved. Therefore, a more facile and elaborate synthesis method need to be explored in order to realize accurate preparation of $ZnIn_2S_4$.
(2) Theory should be combined with experiment more closely in order to unravel the in-depth functional mechanism during reactive process.
(3) More advanced characterization methods and theoretical calculations such as *in-situ* testing should be introduced to shed light on the essential mechanism of photocatalysis.
(4) Novel structures such as Moiré pattern [110] which results from interlacement between the crystalline lattices of $ZnIn_2S_4$ and specific interlayer stacking are still rarely studied, which are expected to be a hotspot in the future.
(5) In a nutshell, $ZnIn_2S_4$ is a promising photocatalyst for energy conversion and environmental remediation. We genuinely hope that this review can provide some new insights into this fascinating material.

Declaration of competing interest

The authors declare that they have no known competing financial interests or personal relationships that could have appeared to influence the work reported in this paper.

Acknowledgments

This work was financially supported by the National Funds for Distinguished Young Scientists (No. 61825503), the Natural Science of China (Nos. 51902101, 61775101 and 61804082), Natural Science of Jiangsu Province (No. BK20201381), and Science of Nanjing University of Posts and Telecommunications (No. NY219144).

References

[1] M.N. Chong, B. Jin, C.W.K. Chow, et al., Water Res. 44 (2010) 2997–3027.
[2] Q. Zhou, Q.H. Bian, L.L. Liao, et al., Chin. Chem. Lett. (2022) 2273–2279.
[3] Q. Zhou, L.L. Liao, H.Q. Zhou, et al., Mater. Today Phys. 26 (2022) 100727.
[4] A. Fujishima, K. Honda, Nature 238 (1972) 37–38.
[5] A. Fujishima, X. Zhang, D.A. Tryk, Surf. Sci. Rep. 63 (2008) 515–582.
[6] H. Zheng, J.Z. Ou, M.S. Strano, et al., Adv. Funct. Mater. 21 (2011) 2175–2196.
[7] J. Fu, Q. Xu, J. Low, et al., Appl. Catal. B: Environ. 243 (2019) 556–565.
[8] J. Zhang, J. Yu, Y. Zhang, et al., Nano Lett. 11 (2011) 4774–4779.
[9] H. Yan, J. Yang, G. Ma, et al., J. Catal. 266 (2009) 165–168.
[10] L. Wang, L. Xie, W. Zhao, et al., Chem. Eng. J. 405 (2021) 127028.
[11] J. Chen, Y. Tang, S. Wang, et al., Chin. Chem. Lett. 33 (2022) 1468–1474.
[12] S. Wang, L. Wang, L. Xie, et al., Nano Res. 15 (2022) 4996–5003.
[13] F. Yu, H.Q. Zhou, Z. Zhu, et al., ACS Catal. 7 (2017) 2052–2057.
[14] K. Maeda, X. Wang, Y. Nishihara, et al., J. Phys. Chem. C 113 (2009) 4940–4947.
[15] P. Niu, L. Zhang, G. Liu, et al., Adv. Funct. Mater. 22 (2012) 4763–4770.
[16] W.J. Ong, L.L. Tan, Y.H. Ng, et al., Chem. Rev. 116 (2016) 7159–7329.
[17] H. Zhou, F. Yu, Y. Huang, et al., Nat. Commun. 7 (2016) 12765.
[18] H. Zhou, Y. Wang, R. He, et al., Nano Energy 20 (2016) 29–36.
[19] J. Wang, S. Sun, R. Zhou, et al., J. Mater. Sci. Technol. 78 (2021) 1–19.
[20] Y. Chen, S. Hu, W. Liu, et al., Dalton Trans. 40 (2011) 2607–2613.
[21] Y. Chen, R. Huang, D. Chen, et al., ACS Appl. Mater. Interfaces 4 (2012) 2273–2279.
[22] X. Chen, L. Liu, P. Yu, et al., Science 331 (2011) 746–750.
[23] Y. Zhou, J. Zhang, E. Song, et al., Nat. Commun. 11 (2020) 2253.
[24] R. Yang, L. Mei, Y. Fan, et al., Small Methods 5 (2021) 2100887.
[25] J. Di, C. Yan, A.D. Handoko, et al., Mater. Today 21 (2018) 749–770.
[26] L.P. Chi, Z.Z. Niu, X.L. Zhang, et al., Nat. Commun. 12 (2021) 5835.
[27] X. Wang, J. Xie, C.M. Li, J. Mater. Chem. A 3 (2015) 1235–1242.
[28] M. Zhang, J. Yao, M. Arif, et al., Appl. Surf. Sci. 526 (2020) 145749.
[29] B. Xu, P. He, H. Liu, et al., Angew. Chem. Int. Ed. 53 (2014) 2339–2343.
[30] T. Su, C. Men, L. Chen, et al., Adv. Sci. 9 (2022) 2103715.
[31] L. Meng, J. He, X. Zhou, et al., Nat. Commun. 12 (2021) 5247.
[32] Y. Zhu, L. Wang, Y. Liu, et al., Appl. Catal. B: Environ. 241 (2019) 483–490.
[33] X. Jiao, Z. Chen, X. Li, et al., J. Am. Chem. Soc. 139 (2017) 7586–7594.
[34] J. Zhou, J. Ding, H. Wan, et al., J. Colloid Interface Sci. 582 (2021) 961–968.
[35] S. Zhang, L. Wang, C. Liu, et al., Water Res. 121 (2017) 11–19.
[36] Y. Zang, S. Niu, Y. Wu, et al., Nat. Commun. 10 (2019) 1217.
[37] Y. Lu, K. Xu, L. Zhang, et al., ACS Nano 14 (2020) 10966–10975.
[38] L. Ye, J. Fu, Z. Xu, et al., ACS Appl. Mater. Interfaces 6 (2014) 3483–3490.
[39] M. Li, J. Su, L. Guo, Int. J. Hydrog. Energy 33 (2008) 2891–2896.
[40] W. Yang, B. Liu, T. Fang, et al., Nanoscale 8 (2016) 18197–18203.
[41] W. Pudkon, H. Bahruji, P.J. Miedziak, et al., Catal. Sci. Technol. 10 (2020) 2838–2854.
[42] X. Gou, F. Cheng, Y. Shi, et al., J. Am. Chem. Soc. 128 (2006) 7222–7229.
[43] P. Hu, S.S. Pramana, S. Cao, et al., Adv. Mater. 25 (2013) 2567–2572.
[44] C. Tan, Z. Lai, H. Zhang, Adv. Mater. 29 (2017) 1701392.
[45] J. Di, J. Xiong, H. Li, et al., Adv. Mater. 30 (2018) 1704548.
[46] M.Q. Yang, Y.J. Xu, W. Lu, et al., Nat. Commun. 8 (2017) 14224.
[47] S. Peng, L. Li, Y. Wu, et al., CrystEngComm 15 (2013) 1922–1930.
[48] S. Shen, L. Zhao, Z. Zhou, et al., J. Phys. Chem. C 112 (2008) 16148–16155.
[49] F. Xing, Q. Liu, C. Huang, Sol. RRL 4 (2020) 1900483.
[50] T. Jia, M. Liu, C. Zheng, et al., Nanomater. Basel 10 (2020) 1–15.
[51] B. Gao, L. Liu, J. Liu, et al., Appl. Catal. B: Environ. 129 (2013) 89–97.
[52] B. Qiu, P. Huang, C. Lian, et al., Appl. Catal. B: Environ. 298 (2021) 120518.
[53] R. Pan, M. Hu, J. Liu, et al., Nano Lett. 21 (2021) 6228–6236.
[54] P. Wang, Z. Shen, Y. Xia, et al., Adv. Funct. Mater. 29 (2019) 1807013.
[55] T. Goswami, D.K. Yadav, H. Bhatt, et al., J. Phys. Chem. Lett. 12 (2021) 5000–5008.
[56] H. Xu, Y. Jiang, X. Yang, et al., Mater. Res. Bull. 97 (2018) 158–168.
[57] W. Yang, L. Zhang, J. Xie, et al., Angew. Chem. Int. Ed. 55 (2016) 6716–6720.
[58] C. Du, B. Yan, Z. Lin, et al., J. Mater. Chem. A 8 (2020) 207–217.
[59] J. Qin, Q. Zhao, Y. Zhao, et al., J. Phys. Chem. C 125 (2021) 23813–23820.
[60] W.K. Chong, B.J. Ng, C.C. Er, et al., Sci. Rep. 12 (2022) 1927.
[61] X. Shi, C. Dai, X. Wang, et al., Nat. Commun. 13 (2022) 1287.
[62] P. Wang, S. Fan, X. Li, et al., Nano Energy 95 (2022) 107045.
[63] C. Feng, X. Yang, Z. Sun, et al., Appl. Surf. Sci. 501 (2020) 144018.
[64] J. Pan, G. Zhang, Z. Guan, et al., J. Energy Chem. 58 (2021) 408–414.
[65] S. Zhang, X. Liu, C. Liu, et al., ACS Nano 12 (2018) 751–758.
[66] S. Shen, X. Chen, F. Ren, et al., Nanoscale Res. Lett. 6 (2011) 290.
[67] W.Y. Lim, M. Hong, G.W. Ho, Dalton Trans. 45 (2016) 552–560.
[68] Y. Fan, R. Yang, J. Zhong, et al., ChemistrySelect 4 (2019) 8815–8821.
[69] N.Q. Yang, J. Li, Opt. Mater. 115 (2021) 111040.
[70] Z. Guan, Z. Xu, Q. Li, et al., Appl. Catal. B: Environ. 227 (2018) 512–518.

[71] L. Lai, F. Xing, C. Cheng, et al., Adv. Mater. Interfaces 8 (2021) 2100052.
[72] L. Tai, Y. Zhou, Ceram. Int. 47 (2021) 32218–32225.
[73] Y. He, H. Rao, K. Song, et al., Adv. Funct. Mater. 29 (2019) 1905153.
[74] Y. Liu, Z. Li, Y. Xie, et al., Mater. Today Chem. 23 (2022) 100714.
[75] S. Zhang, Z. Zhang, Y. Si, et al., ACS Nano 15 (2021) 15238–15248.
[76] Y. Wang, W. Huang, S. Guo, et al., Adv. Energy Mater. 11 (2021) 2102452.
[77] Q. Luan, X. Xue, R. Li, et al., Appl. Catal. B: Environ. 305 (2022) 121007.
[78] G. Zhang, H. Wu, D. Chen, et al., Green Energy Environ. 7 (2022) 176–204.
[79] T. Feng, K. Zhao, H. Li, et al., CrystEngComm 23 (2021) 2547–2555.
[80] X. Wang, X. Wang, J. Huang, et al., Nat. Commun. 12 (2021) 4112.
[81] Y. Qin, H. Li, J. Lu, et al., Appl. Catal. B: Environ. 277 (2020) 119254.
[82] Q. Liu, H. Lu, Z. Shi, et al., ACS Appl. Mater. Interfaces 6 (2014) 17200–17207.
[83] J. Li, C. Wu, J. Li, et al., Chin. J. Catal. 43 (2022) 339–349.
[84] P. Zhang, X.W. Lou, Adv. Mater. 31 (2019) 1900281.
[85] S. Wang, B.Y. Guan, X. Wang, et al., J. Am. Chem. Soc. 140 (2018) 15145–15148.
[86] S. Wang, Y. Wang, S.L. Zhang, et al., Adv. Mater. 31 (2019) 1903404.
[87] H. Fan, Y. Jin, K. Liu, et al., Adv. Sci. 9 (2022) 2104579.
[88] T. Ren, H. Huang, N. Li, et al., J. Colloid Interface Sci. 598 (2021) 398–408.
[89] Y. Xiao, W. Zhang, Q. Xing, et al., Int. J. Hydrog. Energy 45 (2020) 30341–30356.
[90] H. Li, Z.H. Chen, L. Zhao, et al., Rare Metals 38 (2019) 420–427.
[91] Y. Chao, W. Zhang, P. Zhou, et al., Sci. China Chem. 64 (2021) 1716–1722.
[92] H. Su, C. Rao, L. Zhou, et al., Green Chem. 24 (2022) 2027–2035.
[93] H. Li, B. Chong, B. Xu, et al., ACS Catal. 11 (2021) 14076–14086.
[94] Q. Zhang, H. Gu, X. Wang, et al., Appl. Catal. B: Environ. 298 (2021) 120632.
[95] C. Du, B. Yan, G. Yang, Nano Energy 76 (2020) 105031.
[96] Y. Guo, L. Mao, Y. Tang, et al., Nano Energy 95 (2022) 107028.
[97] S. Wang, B.Y. Guan, X.W.D. Lou, J. Am. Chem. Soc. 140 (2018) 5037–5040.
[98] P. She, B. Guan, J. Sheng, et al., Catal. Sci. Technol. 12 (2022) 1092–1099.
[99] Q. Han, L. Li, W. Gao, et al., ACS Appl. Mater. Interfaces 13 (2021) 15092–15100.
[100] B. Pan, Y. Wu, B. Rhimi, et al., J. Energy Chem. 57 (2021) 1–9.
[101] A. Sabbah, I. Shown, M. Qorbani, et al., Nano Energy 93 (2022) 106809.
[102] Z. Yang, X. Xia, W. Yang, et al., Appl. Catal. B: Environ. 299 (2021) 120675.
[103] Y. Lu, X. Jia, Z. Ma, et al., Adv. Funct. Mater. 32 (2022) 2203638.
[104] X. Peng, J. Li, L. Yi, et al., Appl. Catal. B: Environ. 300 (2022) 120737.
[105] C.L. Tan, M.Y. Qi, Z.R. Tang, et al., Appl. Catal. B: Environ. 298 (2021) 120541.
[106] C. Han, G. Han, S. Yao, et al., Adv. Sci. 9 (2022) 2103408.
[107] S. Zhang, Z. Zhang, B. Li, et al., J. Colloid Interface Sci. 586 (2021) 708–718.
[108] R. Yang, Q. Chen, Y. Ma, et al., Chem. Eng. J. 423 (2021) 130164.
[109] S. Chen, X. Zhao, F. Xie, et al., New J. Chem. 44 (2020) 7350–7356.
[110] L. Xie, L. Wang, W. Zhao, et al., Nat. Commun. 12 (2021) 5070.